ASCEND
November 16-18, 2020, Virtual Event
ASCEND 2020

10.2514/6.2020-4243

Quantifying the Impact of Air Drag Models Considering a Rotating Atmosphere in RSO Lifetime Predictions

Ali Hassani* Danielle Racelis† Sandeep K. Jada‡ Jonathan Black§ and Mathieu Joerger¶
Virginia Polytechnic Institute and State University, Blacksburg, VA, 24061

Aaron J. Rosengren‖
University of California, San Diego, California, 92093

This paper provides a comparative analysis of two different atmospheric drag models aimed at predicting the reentry of Resident Space Objects (RSO). We quantify the impact of considering a rotating atmosphere in the drag model, and analyze its effects on the Milankovitch elements, namely the angular momentum vector, and the Laplace-Runge-Lenz vector. The secular variation of the Milankovitch elements is expressed analytically through averaging. We evaluate the performance of the two formulations of the averaged equations of motion to provide accurate predictions of the orbital decay of RSO's, by comparing simulated trajectories to those derived from the non-averaged dynamics, and to a documented spacecraft reentry event. Results show that accounting for atmospheric rotation in the averaged dynamics, provides simulated RSO trajectories closer to the non-averaged dynamics, and to the documented two-line element reentry data.

I. Introduction

Although the impact of atmospheric drag on RSOs has been extensively studied in prior work [1–10], the effect of the rotating atmosphere is not accounted for in some drag models, which can alter the lifetime predictions of the RSOs significantly. The work done in [4] considers a rotating atmospheric model based on Horizontal Wind Model (HWM07) [11], but does not focus on the long-term evolution of the orbits. Recent work in [12] includes a treatment of lifetime predictions of objects in Geo-Synchronous Transfer Orbits (GTOs), by simulating the averaged long-term evolution of atmospheric drag. However, reference [12] does not consider a rotating atmosphere. An approach that accounts for the rotating atmosphere in the drag model is presented by Ward in [13]. Reference [13] builds on prior work with similar formulations [14, 15], but does not assume small eccentricities for ease of analysis. Reference [12] and [13] serve as the main references for this work. A vector treatment is used in deriving the averaged equations, which naturally leads to the description of the orbital geometry in terms of the vectorial elements of the Milankovitch type; namely, the angular momentum vector and the Laplace-Runge-Lenz vector [16].

In this paper, we study the analytical formulation of the averaged equations of motion derived in [12] and [13]. We discuss the fundamental equations, and identify the key differences between the two treatments which include (1) consideration of atmospheric angular velocity, (2) approximations made in evaluating the integrals, and (3) numerical stability. Our focus will be on quantifying the impact that these differences have on simulated trajectories of RSOs. We look specifically at the impact of accounting for a rotating atmosphere versus neglecting relative atmospheric velocity

*Graduate Student, Aerospace and Ocean Engineering Department.
†Graduate Student, Aerospace and Ocean Engineering Department.
‡Graduate Student, Aerospace and Ocean Engineering Department.
§Professor, Aerospace and Ocean Engineering Department; Director, Aerospace and Ocean Systems Laboratory, Hume Center; Co-Director, Center for Space Science and Engineering Research, AIAA Associate Fellow.
¶Assistant Professor, Aerospace and Ocean Engineering Department.
‖Assistant Professor, Mechanical and Aerospace Engineering Department.

in estimating the orbital decay for satellites in GTO. This analysis is carried out by comparing the simulated orbital decay with those obtained from the non-averaged dynamics, and a known reentry event.

In the next section of this paper, the non-averaged equations of motion are derived for RSOs with perturbations due to Earth oblateness, luni-solar third-body gravity, and atmospheric drag. Then, the equations for the averaged dynamics with atmospheric drag are developed with and without atmospheric rotation in Section III. The complete set of averaged equations including J_2 and luni-solar perturbations in addition to atmospheric drag are written out in Section IV. A performance analysis is carried out comparing the two formulations of the averaged equations in Section V. Simulation results are validated against a reference trajectory using the non-averaged dynamics in Section V.C, and against real reentry data in Section V.D. Conclusions are given followed by future work in Section VI. In this preliminary analysis, we perform simulations specifically for objects in GTO. In future work, we will extend this to other orbital regimes.

II. Non-averaged Equations for Perturbed Circumterrestrial Dynamics

In this section, we derive the non-averaged dynamics as a nonlinear relative equation of motion for an RSO with respect to Earth (two-body problem). We first define the unperturbed dynamics considering the Earth and RSO as point masses, with the Earth's gravitational attraction as the primary force acting on the RSO. Later, we model other forces acting on the RSO as perturbations. The perturbations considered in this paper are Earth oblateness, Sun and Moon third-body gravity, and atmospheric drag.

A. Equations of motion

The acceleration of an RSO in Earth's gravity field is defined in Earth Centered Inertial (ECI) frame. The ECI frame is not rotating with respect to Earth, and its x-y plane is the equatorial plane. The x-axis points towards the vernal equinox, and the z-axis is perpendicular to the equatorial plane, and is in the same direction as the Earths spin axis. The y-axis completes the right-hand triad. The RSO acceleration equation can be written as [17]:

$$\ddot{\mathbf{r}} = -\mu \frac{\mathbf{r}}{r^3} + \mathbf{f} \tag{1}$$

$$\mathbf{f} = \mathbf{a}_{J_2} + \mathbf{a}_{S,M} + \mathbf{a}_d \tag{2}$$

where

$\mathbf{r}$	is the position vector of the RSO,
r	is the magnitude of $\mathbf{r}$,
μ	is the Earth's standard gravitational parameter,
$\mathbf{a}_{J_2}$	is the perturbing acceleration due to Earth oblateness,
$\mathbf{a}_{S,M}$	is the perturbing acceleration due to Sun and Moon third-body gravity, and
$\mathbf{a}_d$	is the perturbing acceleration due to atmospheric drag.

The position of the RSO can be found by integrating Eq. (1). When $\mathbf{f} = \mathbf{0}$, the solution to Eq. (1) is a Keplerian orbit and its angular momentum vector is constant. However, when $\mathbf{f} \neq \mathbf{0}$, the solution to Eq. (1) is not a Keplerian orbit, and does not have an exact solution. We can simulate the orbit trajectory by integrating Eq. (1) numerically. If the perturbing accelerations are small enough, the orbital elements vary slowly in time, and the orbit can be described in terms of osculating Keplerian elements.

B. Perturbations model

In this section, we model the perturbing accelerations that cause variations of the angular momentum and specific mechanical energy of the orbit. The RSO trajectory is deviating from the nominal Keplerian orbit because of perturbations, and its lifetime changes correspondingly.

1. Earth oblateness perturbation

Now we relax the assumption that Earth is a point mass. Earth is not a perfect sphere and its density is not uniform. To address this, the Earth's gravitational potential field can be modeled as the sum of spherical harmonic terms. The first term in the summation is already considered in Eq. (1). The second term denoted J_2, models the deviation from the spherical model due to the equatorial bulge, or oblateness of Earth in the equator ($J_2 = 0.0010826267$) [17–19]. The perturbing acceleration due to Earth oblateness can be written as:

$$\mathbf{a}_{J_2} = -\frac{\mu J_2 R^2}{2r^5}\left[\left(1 - \frac{5r_z^2}{r^2}\right)\mathbf{r} + 2r_z\hat{\mathbf{z}}\right] \tag{3}$$

where

R is the mean Earth equatorial radius, and
r_z is the component of $\mathbf{r}$ in the $\hat{\mathbf{z}}$ direction.

Earth oblateness can change an RSO's orbit by rotating its orbital plane around Earth's polar axis (regression of nodes), and also by rotating its orbit in the orbital plane (the advance of the perigee) [17].

2. Luni-Solar third-body gravitational perturbation

The gravitational field of the Sun and Moon impact the trajectory of an RSO. The effects of this third-body perturbation become more significant as the RSO altitude increases. Therefore, at GTO apogees, which can range from tens to hundreds of thousands of kilometers, the luni-solar perturbations' impact is larger than anywhere else on the orbit. It is shown in the literature that at an altitude of one Earth radii the luni-solar perturbation is orders of magnitude smaller than J_2, while at an altitude of 16 Earth radii the magnitude of luni-solar perturbations can be twice as much as J_2. The luni-solar perturbing accelerations can be written as [20]:

$$\mathbf{a}_{S,M} = \mathbf{a}_S + \mathbf{a}_M \tag{4}$$

$$\mathbf{a}_{S/M} = -\mu_{S/M}\left(\frac{\mathbf{d}_{S/M}}{d_{S/M}^3} + \frac{\mathbf{r}_{S/M}}{r_{S/M}^3}\right) \tag{5}$$

$$\mathbf{d}_{S/M} = \mathbf{r} - \mathbf{r}_{S/M} \tag{6}$$

where

$\mu_{S/M}$ is the Sun or Moon gravitational constant,
$\mathbf{r}_{S/M}$ is the position vector of sun or moon in ECI frame, and
$d_{S/M}$ is the magnitude of $\mathbf{d}_{S/M}$.

In this work, the position vectors of the Sun and Moon, $\mathbf{r}_{S/M}$ for any given epoch are calculated based on ephemeris provided by JPL Horizons web interface developed by NASA Jet propulsion Laboratory [21].

3. Drag perturbation

Atmospheric drag can cause changes in RSO trajectory, especially in Low Earth Orbit (LEO). Although drag force decreases significantly at high altitudes (after hundreds of kilometers), it can still change the orbital elements over long periods of time. The impact of atmospheric drag on an RSO's trajectory is well studied in prior work [15, 22]. However, the role of atmospheric rotation in the variation of orbital elements and RSO lifetimes is not as well understood. Therefore, including the Earths atmospheric rotation in the drag model and studying its effects on RSO trajectories is the main contribution of this work. The perturbing drag acceleration including atmospheric rotation can

be expressed as [12, 13]:

$$\mathbf{a}_d = -\frac{1}{2} B\rho |\mathbf{v} - \mathbf{v}_{atm}| \, (\mathbf{v} - \mathbf{v}_{atm}) \tag{7}$$

$$\mathbf{v}_{atm} = \omega_a \hat{\mathbf{z}} \times \mathbf{r} \tag{8}$$

$$B = \text{AMR} \cdot C_d \tag{9}$$

$$\rho = \rho_{p_0} \exp\left(\frac{r_{p_0} - r_p}{H_{\rho_0}}\right) \tag{10}$$

where

$\mathbf{v}_{atm}$	is the linear atmospheric velocity,
ω_a	is the angular atmospheric velocity (considered the same as Earth's spin rate)
$\hat{\mathbf{z}}$	is the unit vector in the direction of the ECI z-axis,
AMR	is the RSO area-to-mass ratio,
C_d	is the RSO drag coefficient,
ρ_{p_0}	is the density at initial perigee altitude,
r_{p_0}	is the initial perigee altitude, and
H_{ρ_0}	is the constant scale height.

Equation (9) is the ballistic coefficient. In many cases, reentering RSOs are tumbling, which results in a time-varying AMR, C_d, and consequently, ballistic coefficients that change over time. In this paper, we consider a constant value for the RSO's AMR, and drag coefficient. However, there is room for improvement by considering a time-varying ballistic coefficient in the simulation. Furthermore, Eq. (10) assumes a spherically symmetric density model for the atmosphere that varies exponentially with altitude. This model is only a function of altitude (r) and does not consider the complexities of solar cycles, space weather, and other spatiotemporal effects of space weather. For consistency in comparing with the averaged results, we use the exponential density model which is analytically defined through averaging. The variables ρ_{p_0} and H_{ρ_0} are calculated based on the 1976 US Standard Atmosphere Model (USSA76).

C. Non-averaged vs averaged dynamics

In the previous sections, we discussed how orbiting objects close to Earth deviate from Keplerian motion as a result of perturbing forces. Fortunately, these deviations are small and their effects are slow, such that we can choose a mean Keplerian orbit whose elements vary slowly with time. The actual orbital motion is oscillatory about this mean, and the mean orbit's period is approximately equal to the actual orbital period. The mean Keplerian orbit is obtained by averaging the perturbed dynamics over a complete period. The resulting singly averaged system no longer has terms that are periodic over one orbital period.

In this paper, we are comparing the performance of the averaged formulations with the non-averaged dynamics. Simulation of the non-averaged dynamics requires numerical integration of the nonlinear equations (1) with all the perturbations. This results in a simulated trajectory that is closer to the true dynamics. The higher fidelity performance of this method is usually achieved at a greater computational cost. In some cases, lifetime analysis for RSOs may involve studying the orbital evolution for tens to thousands of years, and simulating the non-averaged dynamics becomes impractical. Therefore, as an alternative, we can consider only the long-term variations by averaging the rates of change of orbital elements over specific periods of time (discussed in next sections). This approach requires orders of magnitude less computational resources. In this work, for validating the averaging method's performance, the non-averaged dynamics are used as a reference trajectory for short time spans.

The plots in Fig. 1 show a visual comparison of the number of computations for a typical simulation of averaged vs non-averaged trajectories for twelve hours (left plot), and the computational time of the same trajectories for different simulation elapsed times (right plot). The results are produced by a personal computer with 4.00GHz Intel(R) processor with 32.0GB RAM and x64 Windows operating system. We can clearly see that the averaged dynamics outperform the non-averaged dynamics in terms of computational cost.

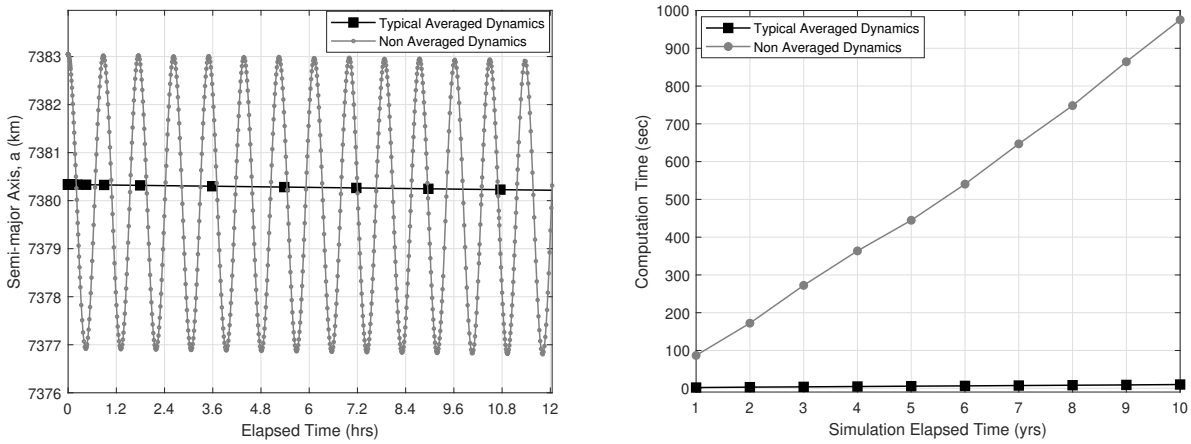

Fig. 1 Computational cost of typical averaged and non-averaged trajectories. Visual comparison of the number of computations (left plot), where each marker shows a computational step, and a comparison of computation time for different simulation time spans (right plot).

III. Averaged Equations for Drag Perturbation

The mean or averaged Keplerian orbit is obtained by averaging the perturbed dynamics over a complete orbital period. The resulting averaged system is autonomous, which means it no longer depends on time. This simplifies the treatment of the problem while providing intuition on the long-term/secular effects of the perturbations on the orbit. We describe the orbital geometry in terms of the Milankovitch elements, angular momentum vector and Laplace-Runge-Lenz vector. This gives the advantage of having to deal with only two vector equations, from which the classical orbital elements can be obtained from without difficulty (see Appendix). The Milankovitch elements are [12]

$$\begin{aligned} \dot{\mathbf{H}} &= \mathbf{r} \times \mathbf{f} \\ \dot{\mathbf{e}} &= \frac{1}{\mu} \left(\mathbf{v} \times \mathbf{r} - \mathbf{H} \right) \times \mathbf{f} \end{aligned} \tag{11}$$

where $\mathbf{H}$ is the instantaneous angular momentum vector given by $\mathbf{r} \times \mathbf{v}$. The eccentricity vector $\mathbf{e}$, points towards the instantaneous argument of perigee and has a magnitude equal to the instantaneous eccentricity of the orbit. The orbital elements are described in the standard ECI frame of reference. The expression for Milankovitch elements given in Eq. (11) is used throughout this work to describe the averaged motion of the perturbed orbits. The averaged dynamics of an RSO over a single orbital period can be derived by integrating with respect to the mean anomaly as below [12].

$$\begin{aligned} \dot{\overline{\mathbf{H}}} &= \frac{1}{2\pi} \int_0^{2\pi} \dot{\mathbf{H}} \, \mathrm{d}M = \frac{1}{2\pi} \int_0^{2\pi} \mathbf{r} \times \mathbf{f} \, \mathrm{d}M \\ \dot{\overline{\mathbf{e}}} &= \frac{1}{2\pi} \int_0^{2\pi} \dot{\mathbf{e}} \, \mathrm{d}M = \frac{1}{2\pi} \int_0^{2\pi} \frac{1}{\mu} \left(\mathbf{v} \times \mathbf{r} - \mathbf{H} \right) \mathbf{f} \, \mathrm{d}M \end{aligned} \tag{12}$$

where the notation $\overline{(\cdot)}$ is used for averaged quantities. In this section we discuss the averaged perturbing acceleration due to atmospheric drag.

A. Averaged drag with a still atmosphere

The drag acceleration on an RSO is given by Eq. (7). With a still atmosphere assumption, $\mathbf{v}_{atm} = 0$, the air drag term can be written as [12]:

$$\mathbf{a}_d = -\frac{1}{2} \rho B v \mathbf{v} \tag{13}$$

where $v = |\mathbf{v}|$. The rates of change of the Milankovitch elements due to drag can be written as follows by substituting Eq. (13) into Eq. (11):

$$\begin{aligned} \dot{\mathbf{H}}_d &= -\frac{1}{2}\rho B v \mathbf{H} \\ \dot{\mathbf{e}}_d &= \frac{1}{\mu}\rho B v \mathbf{H} \times \mathbf{v} \end{aligned} \tag{14}$$

The averaged rates of the **H** and **e** can be obtained by substituting the Eq. (14) into Eq. (12).

$$\begin{aligned} \dot{\overline{\mathbf{H}}}_d &= \frac{1}{2\pi}\int_0^{2\pi}\left(-\frac{1}{2}\rho B v \mathbf{H}\right)\mathrm{d}M = -\frac{1}{2}B\mathbf{H}\frac{1}{2\pi}\int_0^{2\pi}\rho v \mathrm{d}M \\ \dot{\overline{\mathbf{e}}}_d &= \frac{1}{2\pi}\int_0^{2\pi}\left(\frac{1}{\mu}\rho B v \mathbf{H}\times\mathbf{v}\right)\mathrm{d}M = \frac{1}{\mu}B\mathbf{H}\times\left(\frac{1}{2\pi}\int_0^{2\pi}\rho v \mathbf{v}\mathrm{d}M\right) \end{aligned} \tag{15}$$

The exponential density model for ρ was defined in Eq. (10). We get the following expressions for the averaged rates of the Milankovitch elements [12]

$$\dot{\overline{\mathbf{H}}}_d = -\frac{1}{2}B\sqrt{\frac{\mu\left(1-e^2\right)}{2a\pi z}}\rho_{p_0}\exp\left(\frac{r_{p_0}-r_p}{H_{\rho_0}}\right)\left(1+\frac{1+3e^2}{8z\left(1-e^2\right)}\right)\mathbf{H} \tag{16}$$

$$\dot{\overline{\mathbf{e}}}_d = -B\frac{1+e}{a\sqrt{2\pi z}}\rho_{p_0}\exp\left(\frac{r_{p_0}-r_p}{H_{\rho_0}}\right)\left(1+\frac{3e^2-4e-3}{8z\left(1-e^2\right)}\right)H\hat{\mathbf{e}} \tag{17}$$

where $z = \frac{ae}{H_{\rho_0}}$, $r_p = a(1-e)$ is the instantaneous perigee, and H_{ρ_0} is the scale height of the density model in Eq. (10). We refer to the dynamics described in Eq. (16)-(17) as Formulation 1. Note that the directions of **H** and **e** are preserved because the rates of change are in the same direction as the vectors itself. This means that in Formulation 1, the RSO is spiraling into the Earth while the orbital plane is not changing orientation.

B. Averaged drag with a rotating atmosphere

In this section, we derive the averaged drag perturbation considering a finite relative velocity between the satellite and the atmosphere ($\mathbf{v}_{atm} \neq 0$). The averaged drag perturbation with a rotating atmosphere is written from Eq. (7), with $\mathbf{v}_{atm} = \omega_a\hat{\mathbf{z}}\times\mathbf{r}$. Following the derivation in [13], we use the eccentric anomaly E as the variable of integration to arrive at the following equations

$$\dot{\overline{\mathbf{H}}}_d = \frac{Ba}{2T}\int_0^{2\pi}\sqrt{1-e^2\cos^2 E}\left(1-\omega_a\hat{\mathbf{z}}\cdot\frac{\mathbf{H}}{v^2}\right)\left[\mathbf{H}-\omega_a\mathbf{r}\times(\hat{\mathbf{z}}\times\mathbf{r})\right]\rho\ \mathrm{d}E \tag{18}$$

$$\dot{\overline{\mathbf{e}}}_d = \frac{Ba}{2\mu T}\int_0^{2\pi}\sqrt{1-e^2\cos^2 E}\left(1-\omega_a\hat{\mathbf{z}}\cdot\frac{\mathbf{H}}{v^2}\right)\times\left(2\mathbf{H}\times\mathbf{v}-r^2\left(\omega_a\hat{\mathbf{z}}\times\mathbf{v}\right)+\left(\omega_a\hat{\mathbf{z}}\cdot\mathbf{r}\right)\mathbf{H}+\left(\omega_a\hat{\mathbf{z}}\cdot\mathbf{H}\right)\mathbf{r}\right)\rho\ \mathrm{d}E. \tag{19}$$

where $T = 2\pi\sqrt{\frac{a^3}{\mu}}$. The evaluation of these integrals includes much derivation and requires splitting Eq. (18) and (19) into the following four averaged equations for the rates of angular momentum and eccentricity.

$$\dot{\overline{H}}_d = -\frac{BH^2\rho_{p_0}}{2a}\exp\left(\frac{r_{p_0}-a}{H_{\rho_0}}\right)\left[I_0+\frac{H_{\rho_0}e}{2a(1-e^2)}I_1-\frac{2\omega_a a^2\cos i}{H}\left[(1+e^2)I_0-2eI_1\right]\right] \tag{20}$$

$$\dot{\overline{\hat{\mathbf{H}}}}_d = \frac{B\omega_a a\rho_{p_0}}{2}\exp\left(\frac{r_{p_0}-a}{H_{\rho_0}}\right)\left[\left[(1+e^2)I_0-2eI_1\right](\hat{\mathbf{e}}_\perp\cdot\hat{\mathbf{z}})\hat{\mathbf{e}}-\frac{1}{2}(1-e^2)(I_0-I_2)(\hat{\mathbf{e}}\cdot\hat{\mathbf{z}})\hat{\mathbf{e}}_\perp\right]\times\hat{\mathbf{H}} \tag{21}$$

$$\dot{\overline{e}}_d = -\frac{BH\rho_{p_0}}{a}\exp\left(\frac{r_{p_0}-a}{H_{\rho_0}}\right)\left[\left(1-\frac{H_{\rho_0}(2-e^2)}{2a(1-e^2)}\right)I_1+\left(1-\frac{H_{\rho_0}}{2a(1-e^2)}\right)eI_0-\left(\frac{2\omega_a a^2(1-e^2)\cos i}{H}\right)(I_1-eI_0)\right] \tag{22}$$

$$\dot{\overline{\hat{\mathbf{e}}}}_d = -\frac{B\omega_a a\rho_{p_0}}{2}\exp\left(\frac{r_{p_0}-a}{H_{\rho_0}}\right)\left[\frac{1}{2}(1-e^2)(I_0-I_2)(\hat{\mathbf{e}}\cdot\hat{\mathbf{z}})\hat{\mathbf{e}}_\perp\right]\times\hat{\mathbf{H}} \tag{23}$$

where I_0, I_1 and I_2 are modified Bessel functions of the first kind with argument $z = \frac{ae}{H_{\rho_0}}$ of orders 0, 1, and 2 respectively, and $\hat{\mathbf{e}}_\perp = \hat{\mathbf{H}} \times \hat{\mathbf{e}}$. The final vectorial form of the averaged rates of change of the Milankovitch elements are as follows

$$\dot{\overline{\mathbf{H}}}_d = -\frac{BH^2\rho_{p_0}}{2a}\exp\left(\frac{r_{p_0}-a}{H_{\rho_0}}\right)\left[I_0 + \frac{H_{\rho_0}e}{2a(1-e^2)}I_1 - \frac{2\omega_a a^2\cos i}{H}\left[(1+e^2)I_0 - 2eI_1\right]\right]\hat{\mathbf{H}}$$
$$+ \frac{BH\omega_a a\rho_{p_0}}{2}\exp\left(\frac{r_{p_0}-a}{H_{\rho_0}}\right)\left[\left[(1+e^2)I_0 - 2eI_1\right](\hat{\mathbf{e}}_\perp\cdot\hat{\mathbf{z}})\hat{\mathbf{e}} - \frac{1}{2}(1-e^2)(I_0-I_2)(\hat{\mathbf{e}}\cdot\hat{\mathbf{z}})\hat{\mathbf{e}}_\perp\right]\times\hat{\mathbf{H}} \tag{24}$$

$$\dot{\overline{\mathbf{e}}}_d = -\frac{BH\rho_{p_0}}{a}\exp\left(\frac{r_{p_0}-a}{H_{\rho_0}}\right)\left[\left(1-\frac{H_{\rho_0}(2-e^2)}{2a(1-e^2)}\right)I_1 + \left(1-\frac{H_{\rho_0}}{2a(1-e^2)}\right)eI_0 - \left(\frac{2\omega_a a^2(1-e^2)\cos i}{H}\right)(I_1 - eI_0)\right]\hat{\mathbf{e}}$$
$$+ \frac{eB\omega_a a\rho_{p_0}}{2}\exp\left(\frac{r_{p_0}-a}{H_{\rho_0}}\right)\left[\frac{1}{2}(1-e^2)(I_0-I_2)(\hat{\mathbf{e}}\cdot\hat{\mathbf{z}})\hat{\mathbf{e}}_\perp\right]\times\hat{\mathbf{H}} \tag{25}$$

Contrary to the previous model with a still atmosphere, this formulation captures the change in the orbital plane's orientation. The change in direction of $\hat{\mathbf{H}}$ and $\hat{\mathbf{e}}$ given in Eq. (21) and (23) vanishes when the atmospheric angular velocity is zero ($\omega = 0$). We refer to the dynamics described in Eq. (24)-(25) as Formulation 2.

IV. Averaged Equations for J2, and Luni-Solar Third-Body Perturbations

The singly averaged rates of change of $\mathbf{H}$ and $\mathbf{e}$ for J_2 and luni-solar perturbations are given below [12]

$$\begin{aligned}
\dot{\overline{\mathbf{H}}} &= \dot{\overline{\mathbf{H}}}_{J_2} + \dot{\overline{\mathbf{H}}}_S + \dot{\overline{\mathbf{H}}}_M \\
&= -\frac{3\mu J_2 R^2}{2a^3h^5}\left(\hat{\mathbf{z}}\cdot\mathbf{h}\right)\hat{\mathbf{z}}\times\mathbf{h} + \frac{3a^2\mu_S}{2d_S^3}\left[5\left(\hat{\mathbf{d}}_S\cdot\mathbf{e}\right)\mathbf{e}\times\hat{\mathbf{d}}_S - \left(\hat{\mathbf{d}}_S\cdot\mathbf{h}\right)\mathbf{h}\times\hat{\mathbf{d}}_S\right] \\
&\quad + \frac{3a^2\mu_M}{2d_M^3}\left[5\left(\hat{\mathbf{d}}_M\cdot\mathbf{e}\right)\mathbf{e}\times\hat{\mathbf{d}}_M - \left(\hat{\mathbf{d}}_M\cdot\mathbf{h}\right)\mathbf{h}\times\hat{\mathbf{d}}_M\right]
\end{aligned} \tag{26}$$

$$\begin{aligned}
\dot{\overline{\mathbf{e}}} &= \dot{\overline{\mathbf{e}}}_{J_2} + \dot{\overline{\mathbf{e}}}_S + \dot{\overline{\mathbf{e}}}_M \\
&= -\frac{3n\mu J_2 R^2}{4a^2h^5}\left\{\left[1 - \frac{5}{h^2}\left(\hat{\mathbf{z}}\cdot\mathbf{h}\right)^2\right]\mathbf{h}\times\mathbf{e} + 2\left(\hat{\mathbf{z}}\cdot\mathbf{h}\right)\hat{\mathbf{z}}\times\mathbf{e}\right\} \\
&\quad + \frac{3\mu_S}{2nd_S^3}\left[5\left(\hat{\mathbf{d}}_S\cdot\mathbf{e}\right)\mathbf{h}\times\hat{\mathbf{d}}_S - \left(\hat{\mathbf{d}}_S\cdot\mathbf{h}\right)\mathbf{e}\times\hat{\mathbf{d}}_S\right] \\
&\quad + \frac{3\mu_M}{2nd_M^3}\left[5\left(\hat{\mathbf{d}}_M\cdot\mathbf{e}\right)\mathbf{h}\times\hat{\mathbf{d}}_M - \left(\hat{\mathbf{d}}_M\cdot\mathbf{h}\right)\mathbf{e}\times\hat{\mathbf{d}}_M\right]
\end{aligned} \tag{27}$$

where $\mathbf{d}_S$ and $\mathbf{d}_M$ are position vectors from the Earth's center to the centers of Sun and Moon respectively, and $\mathbf{h} = \mathbf{H}/\sqrt{\mu a}$.

There is one caveat to averaging worth mentioning. In averaging, it is assumed that the short-period terms removed by time-averaging cause only small oscillations which do not affect the secular variation of the elements. This will not be true in the presence of resonances [23]. Resonances occur when the period of the orbiting object is a multiple of the period of the forcing term. However, this does not apply to the problem at hand, as will be seen in the scenario that will be presented next.

V. Comparative Analysis of Drag Model Performance

In this section, we compare the performance of the two atmospheric drag models with and without atmospheric rotation, and describe the limitations of each model. We start the section by first looking at simulated trajectories

with atmospheric drag perturbations only. This lets us isolate the effects of atmospheric rotation. Then we add the effects of J_2 and luni-solar third-body gravity, and compare the simulations to those using the non-averaged dynamics. Finally, we quantify the impact of air drag models on RSO lifetime predictions by comparing the simulations with the documented reentry of an Ariane 5 rocket body.

Studying the dynamics and decay of the orbits of spent rocket stages is a prerequisite to responsible mission design [24]. Geo-Synchronous Transfer Orbits (GTOs) are used for transferring satellites from circular low Earth orbit (LEO) to geosyncrhonous Earth orbit (GEO). For this reason, GTOs are highly eccentric orbits, often characterized by a low perigee corresponding to the circular LEO the satellite is transferring from, and a high apogee corresponding to near GEO altitude. We want to analyze the effects of atmospheric drag on the spent rocket stages left uncontrolled at GTO, after the payload has been boosted to GEO. In this preliminary analysis, we perform simulations of the averaged equations specifically for objects in GTO.

For ease of discussion we will refer to the dynamics derived with a still atmosphere in Section III.A as Formulation 1, and those derived considering a rotating atmosphere in Section III.B as Formulation 2 in the legend of subsequent figures.

A. Description of initial conditions

As a baseline for this analysis, the initial orbital elements, area-to-mass ratio (AMR), and drag coefficient were taken to be that of a typical mission profile of Ariane 5. The initial orbital elements defined at GTO injection were given in [12] and repeated below.

$$\begin{aligned} h_{a_0} &= 35,943 \text{ km (apogee altitude)} \\ h_{p_0} &= 250 \text{ km (perigee altitude)} \\ i_0 &= 6^\circ \\ \Omega_0 &= 60^\circ \\ \omega_0 &= 178^\circ \\ \text{AMR} &= 0.02 \text{ m}^2/\text{kg} \\ C_d &= 2.2 \end{aligned} \tag{28}$$

The subscript $(_0)$ in Eq. (28) denotes initial values. The inclination of 6° corresponds to an object launched from a low latitude site, and is a good starting point since these orbits are largely unaffected by the perturbations we will be neglecting when looking at drag only.

B. Simulation results for drag only

Using the initial conditions in Eq. (28), the averaged dynamics for Formulation 1 and 2 were numerically integrated using MATLAB's built-in solver, `ode113` for a time span of 10 years. The following figures show the time history of the classical orbital elements for both Formulations, and for Formulation 2 when $\mathbf{v}_{atm} = 0$.

The plots in Fig. 2 show the in-plane orbital elements a and e monotonically decreasing over time. This means that the orbit is shrinking (decreasing a), and getting more circular (decreasing e). The overlapping results for the thick gray line and the dashed black line, indicate that Formulation 1 is equivalent to Formulation 2 when the atmospheric velocity is set to 0. Going back to Eq. (7), the two drag models differ only by $\mathbf{v}_{atm}$. Consider the case when $\mathbf{v}_{atm} = 0$. A subtle difference between the two sets of equations lies with the approximation of the integrals. These integral approximations should be analytically equivalent, but we find that Formulation 1 is more numerically stable than Formulation 2 for certain initial conditions where the finite accuracy of numerical integration becomes dominant. This comparison of numerical stability is further discussed in Section V.E.

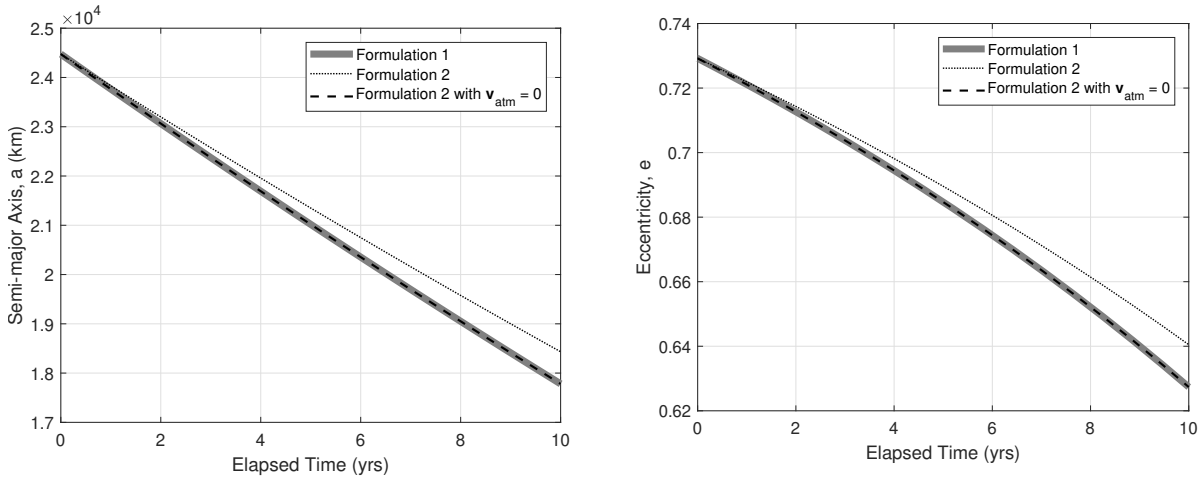

Fig. 2 Time history of the semi-major axis a (left plot), and eccentricity e (right plot) for both atmospheric drag models. The results for Formulation 1 are overlapping with the results for Formulation 2 when $\mathbf{v}_{atm} = 0$.

In Fig. 2, the lines corresponding to zero atmospheric velocity (thick gray, and black dashed lines) have a higher slope than the line corresponding to a finite $\mathbf{v}_{atm}$ (black dotted line). This result implies that for the drag-only case, neglecting atmospheric rotation causes the orbit to decay faster for this set of initial conditions. The time difference for when both orbits decay to 19,000 km is 1 year. We can extrapolate that lifetime prediction discrepancies would be even larger after 10 years. We can inspect this phenomena further by looking at the time histories for the out-of-plane orbital elements.

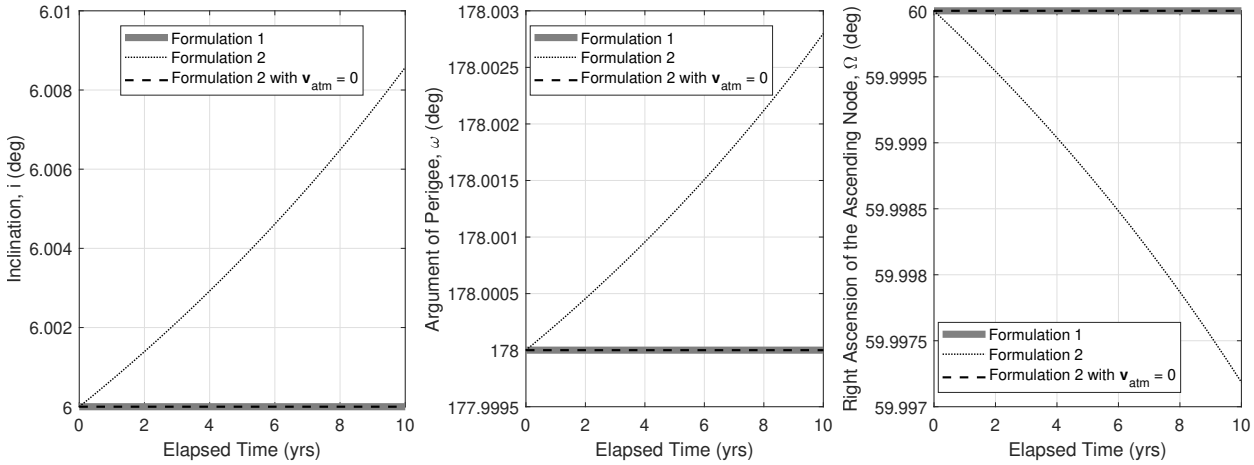

Fig. 3 Time history of inclination i (left plot), argument of perigee ω (center plot), and right ascension of the ascending node Ω (right plot) for both atmospheric drag models. The results for Formulation 1 are overlapping with the results for Formulation 2 when $\mathbf{v}_{atm} = 0$.

In Fig. 3, it is clear that considering atmospheric rotation changes the out-of-plane elements i, and Ω. The secular variation of these elements are small and slow as we can see on the y-axis, but they will not be negligible over long time periods. These variations are due to the fact that drag is a force in the direction anti-parallel to the relative velocity between spacecraft and atmosphere. If we consider a still atmosphere, all the drag force would be in the spacecraft anti-velocity direction. If we consider a rotating atmosphere, the drag force would have out-of-orbit-plane components.

C. Simulation results with drag, J_2, and luni-solar perturbations

Using the same initial conditions as Eq. (28), we now consider the effects of J_2, and luni-solar third-body gravity in addition to drag, and compare simulations with the non-averaged dynamics.

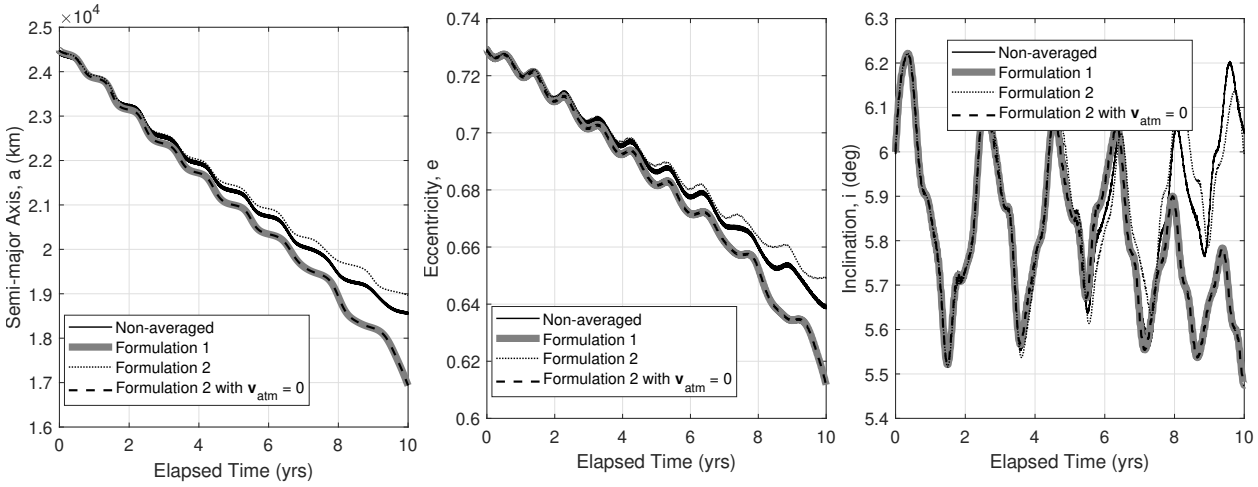

Fig. 4 Time history of the semi-major axis a (left plot), eccentricity e (center plot), and inclination i (right plot) with all perturbations. The results for Formulation 1 are still overlapping with the results for Formulation 2 when $\mathbf{v}_{atm} = 0$ even with all the perturbations.

Figure 4 shows the evolution of a, e, and i for the singly averaged dynamics using Formulation 1 and 2, and the non-averaged dynamics. The linear trend present in the previous figures is now superposed with oscillations from the added perturbations. These additional oscillations have periods corresponding to the orbits between the Earth, Sun, and Moon. Triply averaging about the periods of Earth's orbit about the Sun and Moon would remove these oscillations [12]. The results for the drag model considering atmospheric rotation (dotted black lines) is closer to the non-averaged plots (solid black lines). As expected, the results considering Formulation 1 (dashed black lines) is relatively farther from the non-averaged results. With that in mind, we proceed with just Formulation 2 for the rest of this section.

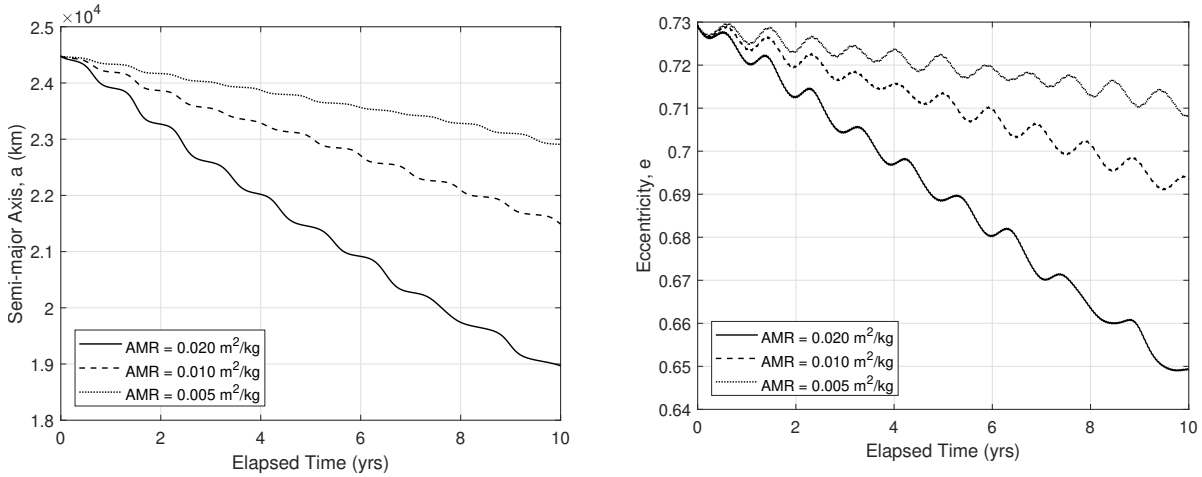

Fig. 5 Time history of the semi-major axis a (left plot), and eccentricity e (right plot). Each line represents the results of a simulation using the area-to-mass-ratio (AMR) indicated in the legend.

In our simulations we use a constant value for the area-to-mass ratio (AMR), while in reality the AMR could be time-varying. So, it is useful to look at a range of AMRs. The subsequent plots show the simulation results using

Formulation 2 for three different values of area-to-mass ratio. The AMR is specified as 0.02, 0.01, and 0.005 m^2/kg, while all other initial conditions were left unchanged. In Fig. 5, we see the same decreasing trend as before for an orbit that is shrinking and getting more circular. From solid, to dashed, to dotted lines, we have decreasing values of AMR. As we expect, higher AMRs incur higher drag force, and these orbits decay faster.

The plots on Fig. 6 show the evolution of perigee altitude h_p and apogee altitude h_a for the three AMR values. The perigee altitude (left plot) is fluctuating around the initial value of 250 km, while the apogee altitude (right plot) is steadily decreasing. This fluctuation is caused by the drag force (which acts as a sort of Δv in the anti-velocity direction) which is much higher at perigee, and less dominant everywhere else on the GTO. The net result is that the orbit is circularizing, and bringing the apogee closer to the focus. These plots show that a slight change in AMR can change the RSO dynamics dramatically. Therefore, comparing the simulations to real data is key to evaluating the performance of the averaged formulations.

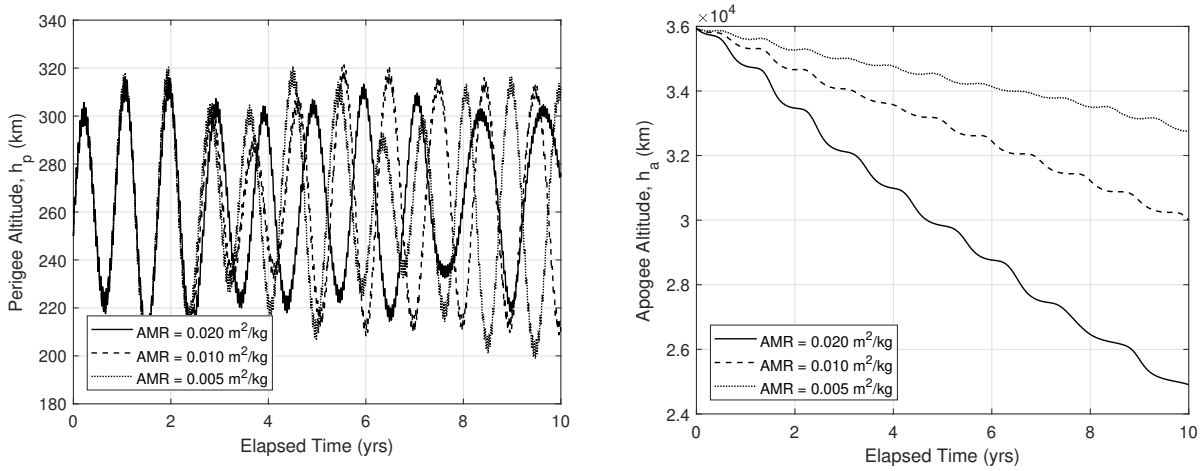

Fig. 6 Time history of perigee altitude h_p (left plot), and apogee altitude h_a (right plot) for Formulation 2. Each line represents the results of a simulation using the area-to-mass-ratio (AMR) indicated in the legend.

D. Comparison with Real Data

In this section, we use the two averaged formulations and the non-averaged dynamics to simulate the trajectory of Ariane 5 R/B (NORAD ID:37239) which launched on November 25, 2010, and reentered the atmosphere on August 15, 2014. The "true" trajectory is retrieved in the form of Two-Line Elements (TLE) from space-track.org [25]. Despite uncertainties in the TLE data, its limited accuracy is sufficient for this study [26]. The set of initial conditions used for this set of simulations are as follows:

$$\begin{aligned} h_{a_0} &= 35,730.611 \text{ km (apogee altitude)} \\ h_{p_0} &= 238.181 \text{ km (perigee altitude)} \\ i_0 &= 1.750^\circ \\ \Omega_0 &= 180.581^\circ \\ \omega_0 &= 168.584^\circ \end{aligned} \tag{29}$$

In the previous section, we showed how a small change in AMR (and consequently the ballistic coefficient) can significantly change the predicted dynamics. In addition, the perturbations neglected in the formulation of the averaged dynamics will introduce errors when compared to the TLE data.

To address these issues, the first step in this performance analysis is determining an acceptable estimate of the ballistic coefficient. We accomplish this step by doing a sensitivity analysis on the ballistic coefficient using a high-fidelity non-averaged dynamic model which includes drag, J_2, luni-solar third-body perturbations, solar radiation pressure, third body perturbations from other planets, Earth's solid tides, ocean tides, and relativity perturbations [27]. Once the ballistic coefficient is determined, we run the non-averaged dynamics with just drag, J_2, and luni-solar perturbations, consistent with the averaged formulations. This step allows us to determine the lifetime prediction discrepancy caused by neglecting other perturbations, before making observations on the error caused by the atmospheric drag models. Figure 7 shows the evolution of semi-major axis with different ballistic coefficients. For compactness, only the semi-major axis time history is shown here. The ballistic coefficient $B = 0.0106$ yields the closest trajectory to the TLE data, and will be used in subsequent analysis.

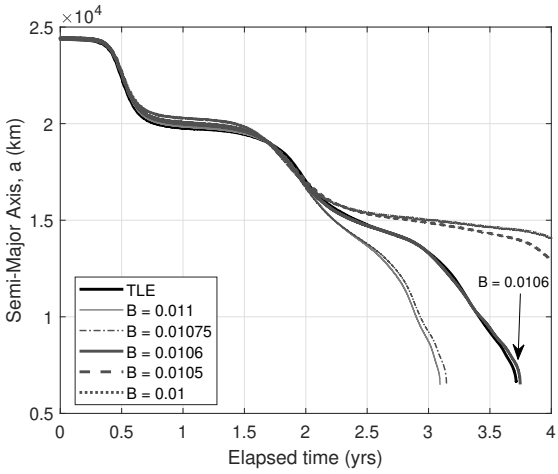

Fig. 7 Time history of semi-major axis a for varying ballistic coefficients simulated using the high-fidelity non-averaged dynamics.

Figure 8 compares the time history of the perigee altitude simulated using the non-averaged and averaged dynamics, against the TLE data (solid black line). The results simulated using the high-fidelity non-averaged model (light gray line) is the closest to the TLE. Reducing the non-averaged model to consider only atmospheric drag, J_2 and luni-solar perturbations already introduces a discrepancy of ~ 1.5 years in the reentry prediction (dark gray line). By averaging we introduce ~ 3 years of additional error (dotted line). Furthermore, neglecting atmospheric rotation in Formulation 2 causes another $\sim$3 years error in reentry (dashed line). As expected, Formulation 2 which accounts for atmospheric rotation has better performance than Formulation 2 without atmospheric rotation (matches with Formulation 1). Although the results of both averaged formulations are off from the true reentry trajectory, this figure quantifies the relative performance between considering atmospheric rotation and neglecting it in the averaged dynamics. In addition, the advantage of using the averaged equations lies with times scales much larger than the one presented here. Further performance analysis using longer time scales, and considering additional perturbations in the averaged dynamics could be pursued in future work.

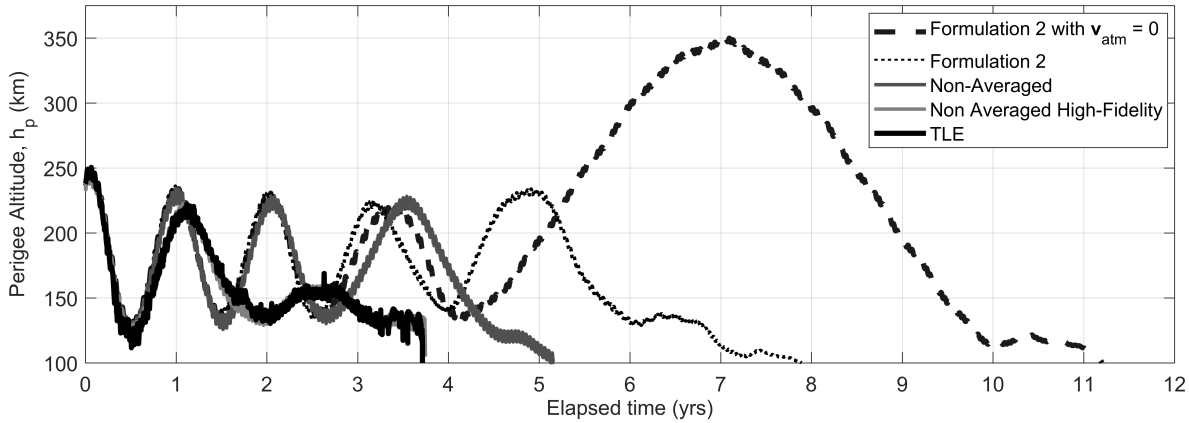

Fig. 8 Time history of perigee altitude h_p for both averaged formulations, non-averaged dynamics, and high-fidelity non-averaged dynamics, compared against TLE data for Ariane 5 R/B (NORAD ID: 37239). The results for Formulation 1 and Formulation 2 with $\mathbf{v}_{atm} = 0$ match very closely, so only Formulation 2 with $\mathbf{v}_{atm} = 0$ is shown here.

E. Numerical stability analysis of Formulation 2: averaged drag dynamics with a rotating atmosphere

There are terms in Formulation 2 of the averaged drag perturbation [13] which can cause numerical issues. These issues arise for certain initial conditions. In the equations of motion given in Eq. (20)-(25), the density-like term $\rho_{p_0}\exp\left(\frac{r_{p_0}-a}{H_\rho}\right)$ can be rewritten using the relationship between perigee altitude and semi-major axis as follows:

$$\begin{aligned}\rho_{p_0}\,\exp\left(\frac{r_{p_0}-a}{H_{\rho_0}}\right) &= \rho_{p_0}\,\exp\left(\frac{r_{p_0}-(r_p+ae)}{H_{\rho_0}}\right)\\ &= \rho_{p_0}\,\exp\left(\frac{r_{p_0}-r_p}{H_{\rho_0}}\right)\,\exp\left(-\frac{ae}{H_{\rho_0}}\right)\\ &= \rho\;\exp\left(-\frac{ae}{H_{\rho_0}}\right)\end{aligned} \tag{30}$$

resulting in the density model given in Eq. (10) multiplied by the term $\exp\left(-\frac{ae}{H_{\rho_0}}\right)$, where $z = \frac{ae}{H_{\rho_0}}$ as defined in Section III.A. When Eq. (30) is distributed out to terms in Eq. (20) to (25), we get expressions containing the following products

$$\exp(-z)\;I_0(z), \quad \exp(-z)\;I_1(z), \quad \exp(-z)\;I_2(z) \tag{31}$$

where z is the argument of the Bessel function $I_\nu(.)$. Although theoretically the products in Eq. (31) yield values between zero and one, $\exp(-z)$ and $I_\nu(z)$ respectively return the smallest and largest numbers that can be represented by double precision floating-point numbers (1e-308 is numerically zero and 1e+308 is numerically ∞). As a result, when the equations are evaluated beyond $z = 700$ we get '0' times 'Inf' which is 'Not a Number'. Figure 9 plots the first term in Eq. (31) as a function of z.

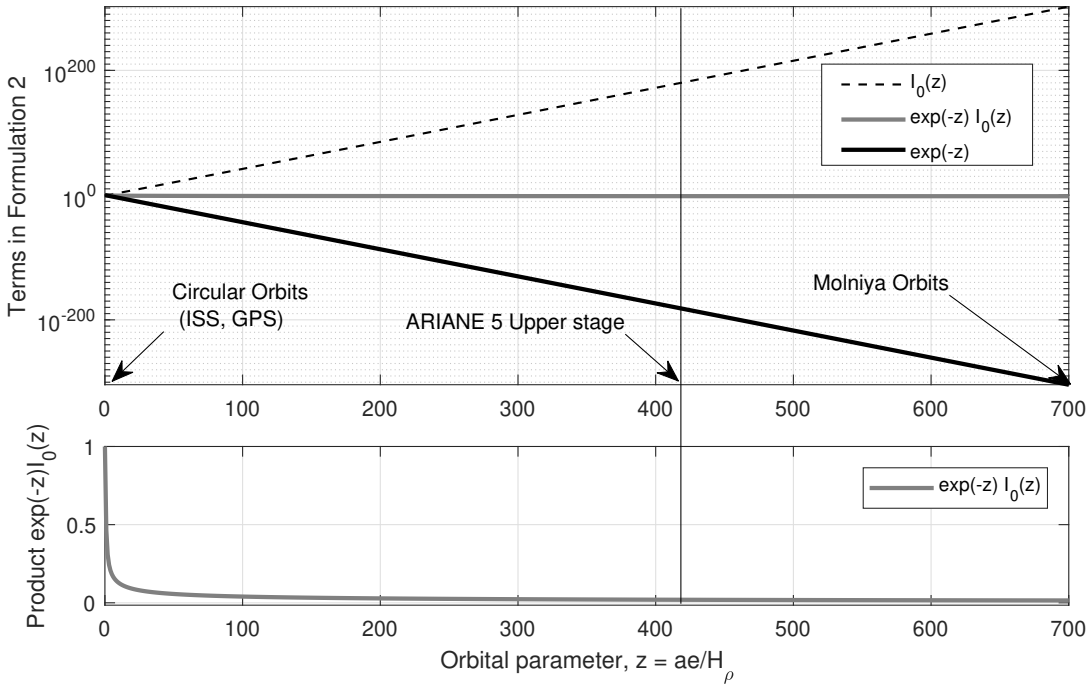

Fig. 9 Variation of the modified Bessel function I_0, negative exponential term, and their product are plotted on a log scale on the top plot. The product term $\exp(-z)I_0(z)$ is plotted on a linear scale on the bottom plot. For values beyond 700, the terms evaluated are outside the range of double-precision floating-point arithmetic.

The product terms in Eq. (31) vary between 1 for near circular orbits, and a very small number for highly elliptic orbits. For large arguments of z, we can approximate the modified Bessel functions in Eq. (31) with an asymptotic expansion as follows [28]

$$I_\nu(z) \sim \frac{\exp(z)}{\sqrt{2\pi z}}\left[1 - \frac{\alpha-1}{8z} + \frac{(\alpha-1)(\alpha-3)}{2!(8z)^2} - \frac{(\alpha-1)(\alpha-9)(\alpha-25)}{3!(8z)^3} + ...\right] \tag{32}$$

where $\alpha = 4\nu^2$. Then for large values of z the terms in Eq. (31) become

$$\exp(-z)I_\nu(z) \sim \frac{1}{\sqrt{2\pi z}}\left[1 - \frac{\alpha-1}{8z} + \frac{(\alpha-1)(\alpha-3)}{2!(8z)^2} - \frac{(\alpha-1)(\alpha-9)(\alpha-25)}{3!(8z)^3} + ...\right]. \tag{33}$$

The expression in Eq. (33) is free of numerical issues and can be evaluated with increasing accuracy by considering higher order terms. This approximation is used for the simulation of an example RSO in GTO. Fig. 10 shows the evolution a and e for Ariane 4LP upper-stage rocket body. The initial value of the orbital parameter z is 801.39. At this value of z, the Bessel function $I_\nu(z)$, and the exponential function $\exp(-z)$ fall outside the double-precision floating-point arithmetic range of most software. Using the approximation in Eq. (33), we are able to simulate the dynamics of Formulation 2 from Section III.B which was not possible otherwise.

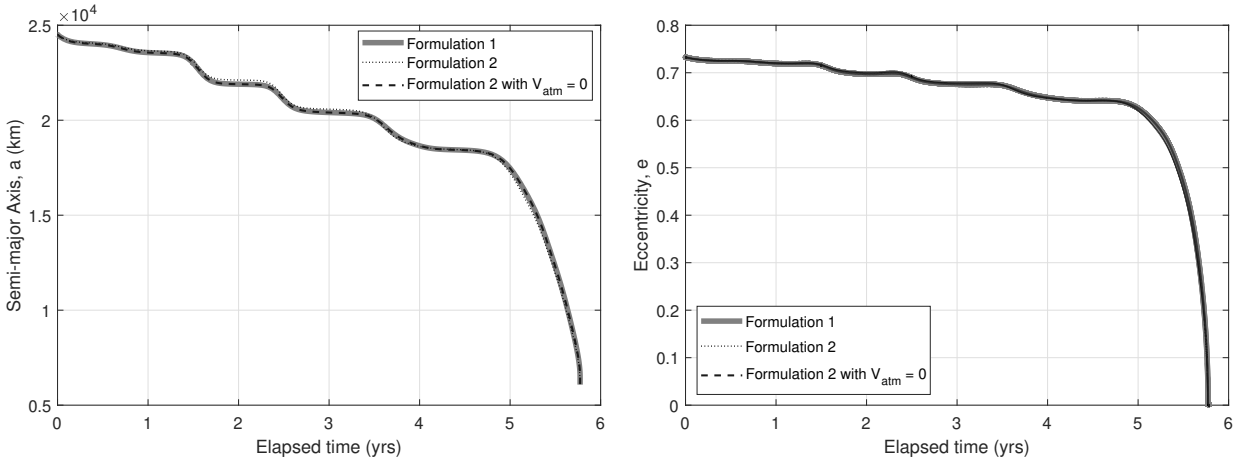

Fig. 10 Time history of the semi-major axis a (left plot), and eccentricity e (right plot) with all perturbations for Ariane 4LP upper-stage R/B (NORAD ID:19218) with orbital parameter, $z = 801.39$

VI. Conclusions

Simulating the non-averaged equations is computationally expensive, therefore, for applications requiring long propagation intervals, it is advantageous to use the averaged equations. This paper analyzed the secular variation of the Milankovitch elements for an RSO in GTO (1) under the influence of atmospheric drag alone, and (2) under the influence of atmospheric drag with J_2 and luni-solar perturbations.

We showed the impact of considering atmospheric rotation by comparing two models, Formulation 1 which considers a still atmosphere, and Formulation 2 which considers a rotating atmosphere. Results show that the two models are equivalent when atmospheric rotation is set to zero for Formulation 2, using the given set of initial conditions, and assuming no numerical issues. Since drag is a function of relative velocity between the atmosphere and the RSO, neglecting atmospheric rotation only accounts for the in-plane components of the drag force. In contrast, Formulation 2 captures the out-of-orbit-plane drag components, thus affecting the out-of-plane elements, and changing the orientation of the orbit plane.

We showed that Formulation 2 is numerically ill-conditioned, and we proposed a numerically stable approximation as outlined in Section V.E. In addition, we showed the effect of varying AMR on lifetime predictions using Formulation 2. Finally, we evaluated the performance of the averaged formulations by comparing them to a known reentry event. Formulation 2, which accounts for a rotating atmosphere, gave results that are closer to the reference non-averaged dynamics and correspondingly to the TLE data.

Appendix

From the classical orbital elements, we compute the Milankovitch elements, **H** and **e** through the equations below.

$$r_a = h_a + R \quad , \quad r_p = h_p + R \quad , \quad a = \frac{1}{2}(r_a + r_p) \quad , \quad e = 1 - \frac{r_p}{a} \quad , \quad H = \sqrt{a\mu(1-e^2)} \tag{34}$$

$$\hat{\mathbf{H}} = \sin\Omega \sin i\ \hat{\mathbf{x}} - \cos\Omega \sin i\ \hat{\mathbf{y}} + \cos i\ \hat{\mathbf{z}} \tag{35}$$

$$\hat{\mathbf{e}} = (\cos\omega\cos\Omega - \cos i\ \sin\omega\sin\Omega)\hat{\mathbf{x}} + (\cos\omega\sin\Omega + \cos i\ \sin\omega\cos\Omega)\hat{\mathbf{y}} + \sin\omega\sin i\ \hat{\mathbf{z}} \tag{36}$$

From these definitions, the Milankovitch elements are

$$\mathbf{H} = H\,\hat{\mathbf{H}}\,, \tag{37}$$

$$\mathbf{e} = e\ \hat{\mathbf{e}}\,. \tag{38}$$

The equations used to retrieve the classical orbital elements from the Milankovitch elements are listed below.

$$e = |\mathbf{e}| \quad , \quad a = \frac{H^2}{\mu(1-e^2)} \quad , \quad i = \cos^{-1}(\hat{\mathbf{z}}\cdot\hat{\mathbf{H}}) \quad , \quad \Omega = \sin^{-1}\left(\frac{\hat{\mathbf{x}}\cdot\hat{\mathbf{H}}}{|\hat{\mathbf{z}}\times\hat{\mathbf{H}}|}\right) \quad , \quad \omega = \cos^{-1}\left(\frac{\mathbf{e}\cdot(\hat{\mathbf{z}}\times\hat{\mathbf{H}})}{e|\hat{\mathbf{z}}\times\hat{\mathbf{H}}|}\right) \tag{39}$$

References

[1] de Lafontaine, J., and Garg, S. C., "A Review of Satellite Lifetime and Orbit Decay Prediction," *Indian Academy of Sciences Proceedings: Section C Engineering Sciences*, Vol. 5, 1982, pp. 197–258.

[2] Fu, X., Wu, M., and Tang, Y., "Design and Maintenance of Low-Earth Repeat-Ground-Track Successive-Coverage Orbits," *Journal of Guidance, Control, and Dynamics*, Vol. 35, No. 2, 2012, pp. 686–691. https://doi.org/10.2514/1.54780, URL https://doi.org/10.2514/1.54780.

[3] Peng, H., and Bai, X., "Artificial Neural NetworkBased Machine Learning Approach to Improve Orbit Prediction Accuracy," *Journal of Spacecraft and Rockets*, Vol. 55, No. 5, 2018, pp. 1248–1260. https://doi.org/10.2514/1.A34171, URL https://doi.org/10.2514/1.A34171.

[4] Zhang, R., Han, C., Sun, X., and Qi, Z., "Initial Orbit Determination from Atmospheric Drag Direction," *Journal of Guidance, Control, and Dynamics*, Vol. 42, No. 12, 2019, pp. 2731–2740. https://doi.org/10.2514/1.G004530, URL https://doi.org/10.2514/1.G004530.

[5] Morand, V., Fèvre, C., Lamy, A., Fraysse, H., and Deleflie, F., "Dynamical Properties of Geostationary Transfer Orbits Over Long Time Scales: Consequences for Mission Analysis and Lifetime Estimation," 2012, pp. 1–2. https://doi.org/10.2514/6.2012-4968.

[6] David, E., and Braun, V., "Re-Entry Analysis Comparison with Different Solar Activity Models of Spent Upper Stage Using ESA's DRAMA Tool," *Safety is Not an Option, Proceedings of the 6th IAASS Conference*, ESA Special Publication, Vol. 715, 2013, p. 15.

[7] Shute, B. E., "Pre-Launch Analysis of High Eccentricity Orbits," NASA Technical Note D-494, Jan. 1964.

[8] Cook, G., and Scott, D. W., "Lifetimes of Satellites in Large-Eccentricity Orbits," *Planetary and Space Science*, Vol. 15, No. 10, 1967, pp. 1549 – 1556. https://doi.org/https://doi.org/10.1016/0032-0633(67)90088-8, URL http://www.sciencedirect.com/science/article/pii/0032063367900888.

[9] Janin, G., "Decay of Debris in Geostationary Transfer Orbit," *Advances in Space Research*, Vol. 11, No. 6, 1991, pp. 161 – 166. https://doi.org/https://doi.org/10.1016/0273-1177(91)90247-H, URL http://www.sciencedirect.com/science/article/pii/027311779190247H.

[10] Bettinger, R. A., Black, J. T., Agte, J. S., and Spencer, D., "Design of Experiment Approach to Atmospheric Skip Entry Maneuver Optimization," *Journal of Spacecraft and Rockets*, Vol. 52, No. 3, 2015, pp. 813–826. https://doi.org/10.2514/1.A33032.

[11] Drob, D. P., Emmert, J. T., Crowley, G., Picone, J. M., Shepherd, G. G., Skinner, W., Hays, P., Niciejewski, R. J., Larsen, M., She, C. Y., Meriwether, J. W., Hernandez, G., Jarvis, M. J., Sipler, D. P., Tepley, C. A., O'Brien, M. S., Bowman, J. R., Wu, Q., Murayama, Y., Kawamura, S., Reid, I. M., and Vincent, R. A., "An Empirical Model of the Earth's Horizontal Wind Fields: HWM07," *Journal of Geophysical Research: Space Physics*, Vol. 113, No. A12, 2008. https://doi.org/10.1029/2008JA013668, URL https://agupubs.onlinelibrary.wiley.com/doi/abs/10.1029/2008JA013668.

[12] Wang, Y., and Gurfil, P., "Dynamical Modeling and Lifetime Analysis of Geostationary Transfer Orbits," *Acta Astronautica*, Vol. 128, 2016, pp. 262–276. https://doi.org/10.1016/j.actaastro.2016.06.050.

[13] Ward, G. N., "On the Secular Variations of the Elements of Satellite Orbits," *Royal Society of London. Series A, Mathematical and Physical Sciences*, Vol. 266, No. 1324, 1962, pp. 266–130. https://doi.org/10.1086/104968.

[14] Musen, P., "Special Perturbations of the Vectorial Elements," *The Astronomical Journal*, Vol. 59, 1954, pp. 262–267.

[15] Allan, R. R., "Satellite Orbit Perturbations in Vector Form," *Nature*, Vol. 190, 1961, p. 615.

[16] Rosengren, A. J., and Scheeres, D. J., "On the Milankovitch Orbital Elements for Perturbed Keplerian Motion," *Celestial Mechanics and Dynamical Astronomy*, Vol. 118, No. 3, 2014, pp. 197–220. https://doi.org/10.1007/s10569-013-9530-7.

[17] Wiesel, W. E., *Spaceflight Dynamics*, 3rd ed., Aphelion Press, Beavercreek, Ohio, 2012.

[18] Vallado, D., and McClain, W., *Fundamentals of Astrodynamics and Applications*, 4th ed., Microcosm Press, Hawthorne, Calif, 2007.

[19] Hassani, A., Saghafi, F., and Pasand, M., "H_∞ and μ Synthesis Control of Virtual Structure Satellites Formation Flying," *International Journal of Dynamics and Control*, Vol. 5, 2016, pp. 741–755. https://doi.org/10.1007/s40435-016-0238-x.

[20] Roy, A. E., "Luni-solar perturbations of an Earth satellite," *Astrophys Space Sci*, Vol. 4, 1969, p. 375386. https://doi.org/https://doi.org/10.1007/BF00651343.

[21] Jet Propulsion Laboratory, "Horizons Web Interface," , 2020. URL https://ssd.jpl.nasa.gov/horizons.cgi.

[22] Roy, A. E., and Moran, P. E., "Studies in the Application of Recurrence Relations to Special Perturbation Methods," *Celestial Mechanics*, Vol. 7, 1973, pp. 236–255.

[23] Skoulidou, D. K., Rosengren, A. J., Tsiganis, K., and Voyatzis, G., "Dynamical Lifetime Survey of Geostationary Transfer Orbits," *Celestial Mechanics and Dynamical Astronomy*, Vol. 130, No. 11, 2018, p. 77.

[24] Pasand, M., Hassani, A., and Ghorbani, M., "A Comprehensive Study of Reaction Control Thrusters Configurations for 3-axis Upper Stage Attitude Control ," *IEEE Aerospace and Electronic Systems Magazine*, Vol. 32, No. 7, 2017, pp. 22–39. https://doi.org/10.1109/MAES.2017.160104.

[25] SPACE-TRACK.ORG, 2020. URL http://www.space-track.org/.

[26] Racelis, D., and Joerger, M., "High-Integrity TLE Error Models for MEO and GEO Satellites," *2018 AIAA SPACE and Astronautics Forum and Exposition*, 2018. https://doi.org/10.2514/6.2018-5241.

[27] Mahooti, M., "Satellite Orbit Modeling," 2020. URL https://www.mathworks.com/matlabcentral/fileexchange/54877-satellite-orbit-modeling, Retrieved September 25, 2020.

[28] Abramowitz, M., Stegun, I. A., and Romer, R. H., *Handbook of Mathematical Functions with Formulas, Graphs, and Mathematical Tables*, American Association of Physics Teachers, 1988.